Axon initial segment dysfunction in a mouse model of genetic epilepsy with febrile seizures plus

Verena C. Wimmer,[1] Christopher A. Reid,[1,2] Suzanne Mitchell,[1] Kay L. Richards,[1] Byron B. Scaf,[1] Bryan T. Leaw,[1] Elisa L. Hill,[1] Michel Royeck,[3] Marie-Therese Horstmann,[3,4,5] Brett A. Cromer,[1] Philip J. Davies,[1] Ruwei Xu,[1] Holger Lerche,[6,7] Samuel F. Berkovic,[8] Heinz Beck,[3] and Steven Petrou[1,2]

[1]Florey Neuroscience Institutes and [2]The Centre for Neuroscience, The University of Melbourne, Parkville, Victoria, Australia. [3]Department of Epileptology, University of Bonn Medical Center, Bonn, Germany. [4]Helmholtz-Institute for Radiation and Nuclear Physics and [5]Interdisciplinary Center for Complex Systems, University of Bonn, Bonn, Germany. [6]Neurologische Klinik und Institut für Angewandte Physiologie der Universität Ulm, Zentrum Klinische Forschung, Ulm, Germany. [7]Abteilung Neurologie mit Schwerpunkt Epileptologie, Hertie-Institut für klinische Hirnforschung, Universitätsklinikum Tübingen, Tübingen, Germany. [8]Epilepsy Research Centre, The University of Melbourne, Austin Health, Heidelberg West, Victoria, Australia.

Febrile seizures are a common childhood seizure disorder and a defining feature of genetic epilepsy with febrile seizures plus (GEFS+), a syndrome frequently associated with Na^+ channel mutations. Here, we describe the creation of a knockin mouse heterozygous for the C121W mutation of the β1 Na^+ channel accessory subunit seen in patients with GEFS+. Heterozygous mice with increased core temperature displayed behavioral arrest and were more susceptible to thermal challenge than wild-type mice. Wild-type β1 was most concentrated in the membrane of axon initial segments (AIS) of pyramidal neurons, while the β1(C121W) mutant subunit was excluded from AIS membranes. In addition, AIS function, an indicator of neuronal excitability, was substantially enhanced in hippocampal pyramidal neurons of the heterozygous mouse specifically at higher temperatures. Computational modeling predicted that this enhanced excitability was caused by hyperpolarized voltage activation of AIS Na^+ channels. This heat-sensitive increased neuronal excitability presumably contributed to the heightened thermal seizure susceptibility and epileptiform discharges seen in patients and mice with β1(C121W) subunits. We therefore conclude that Na^+ channel β1 subunits modulate AIS excitability and that epilepsy can arise if this modulation is impaired.

Introduction

Na^+ channels play vital roles in many aspects of neuronal function, from subthreshold signaling and encoding of information via action potential (AP) initiation and propagation to synaptic transmission and control of brain oscillations. To accommodate this functional diversity, Na^+ channels are subject to an array of modulatory influences, notably by β accessory subunits (1, 2), of which 4 have been identified.

β1, in particular, is of considerable interest because mutations in the *SCN1B* gene cause human epilepsy (3–5), particularly the syndrome of genetic (generalized) epilepsy with febrile seizures (FS) plus (GEFS+). In vitro studies of the human epilepsy mutation β1(C121W) suggest a disease mechanism caused by loss of modulatory function (6, 7). Translation of these findings into neuronal disease mechanisms has proven to be elusive because of our limited understanding of β1 neurobiology. While β1 coexpression has been shown in some studies to modulate Na^+ channel function, these findings are somewhat inconsistent (3, 8–12). Furthermore, a recent publication was able to demonstrate β1 localization in the axon initial segments (AIS) of cerebellar neurons (13), but the lack of a clear picture of cellular β1 expression patterns in different brain regions is still contributing to our poor understanding of the role of β1 in epileptogenesis (14, 15).

β1 homozygous knockout animals die at around P20 (16), leaving little doubt that β subunits are vital. Nonetheless, these studies have fallen short of defining a precise neuronal or in vivo physiological function (5, 16, 17). We present a knockin mouse model of the β1(C121W) epilepsy mutation that not only sheds light on the in vivo role of wild-type β1 but also provides what we believe is a novel disease mechanism. Heterozygous mice show increased propensity to thermally triggered seizures, analogous to FS seen in human patients carrying the β1(C121W) mutation (3, 4). We demonstrate that the wild-type subunit is localized to the AIS, the site of AP initiation (13, 18–21), and importantly, the β1(W121) mutant is excluded from the membrane of this neuronal compartment. Current clamp recordings revealed increased excitability in neurons of mice heterozygous for the β1(C121W) mutation caused by a temperature-sensitive change in AIS function.

Results

Construction of the mouse model. Knockin mice harboring the β1(C121W) mutation (C387G transversion in exon 3 of genomic sequence) (3) were generated by homologous recombination in mouse embryonic stem cells (Figure 1, A and B; see Methods).

To ensure that the β1(C121W) mutation did not lead to degradation of β1 in vivo, we performed Western blot analysis using a custom-made antibody (see Methods). The antibody specifically recognized β1-EGFP fusion proteins in transfected HEK cells (Figure 1C). Whole-brain extracts of P16 WW [homozygous for the β1(C121W) mutation], CC (wild-type), and CW (heterozygous)

Conflict of interest: S.F. Berkovic and S. Petrou were paid consultants for Bionomics Ltd., which owns the intellectual property rights related to the knockin mouse described in this study.

Citation for this article: *J Clin Invest.* 2010;120(8):2661–2671. doi:10.1172/JCI42219.

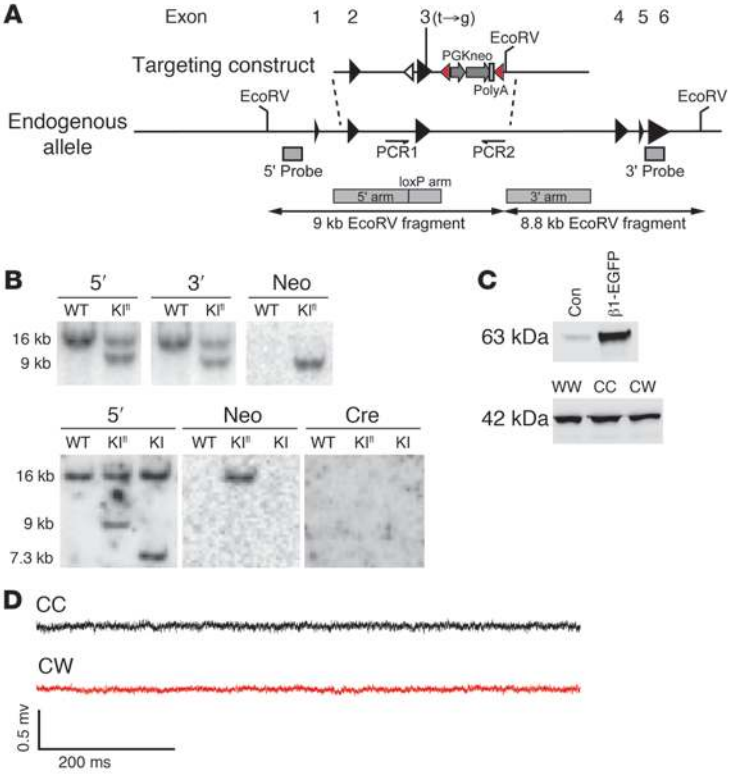

Figure 1
Construction of the CW mouse model. (**A**) Targeting strategy for creating of the β1(C121W) knockin mouse model. Black triangles, *Scn1b* exons; white and red triangles, loxP sites; gray arrows, PKG/neo cassettes. Recombination between the 2 loxP sites highlighted in red led to generation of CW knockin mice. (**B**) Top panel: Southern blot analysis showing correct genomic targeting of the floxed cassette (KI^{fl}) using 5′ (left), 3′ (middle), and Neo (right) probes. Bottom panel: Southern blot analysis of PGKneo excision and retention of exon3 carrying the C121W mutation. The blot shown in the left image was stripped and reprobed for Neo (expected band size: approximately 16 kb, middle) and Cre (expected band size: approximately 10 kb, right). (**C**) Western blots. Top panel: untransfected control HEK cells and HEK cells transfected with cDNA coding for mouse β1-EGFP. Bottom panel: whole-brain extracts of P16 WW, CC, and CW mutant mice. Identical protein levels in all 3 genotypes. (**D**) Normal ECoGs in somatosensory cortex of P37 CC (black) and CW mice (red).

mice showed identical β1 protein levels, suggesting that the mutation did not reduce protein levels (Figure 1C).

CW mice were viable and fertile with normal electrocorticograms (ECoG), gross neuroanatomy, growth, and survival (Figure 1D and Supplemental Figure 1; supplemental material available online with this article; doi:10.1172/JCI42219DS1). WW mice showed a severe phenotype and usually died before P25.

Heterozygous CW mice have a FS phenotype. FS are the major clinical presentation in patients heterozygous for the β1(C121W) mutation and occur in more than 80% of subjects, typically in the second year of life and often in combination with a variety of other seizure types as part of the syndrome GEFS+ (3, 4, 22). To assess the "FS" phenotype of CW mice, we increased the core temperature by exposing the animals to a warm stream of air while simultaneously recording video, ECoG, and hippocampal field potentials (Figure 2A). With increasing temperature, all mice displayed behavioral arrest, facial automatisms, and early epileptiform discharges localized to the hippocampus, as described previously for rat models of thermal seizures (Figure 2A) (23, 24). In WW mice, these thermal seizures rapidly evolved into severe tonic-clonic seizures (n = 25). Intriguingly, the average threshold temperature for behavioral arrest was lowered by 0.44 ± 0.17°C in heterozygous CW mice and by 1.2 ± 0.15°C in homozygous WW mice relative to CC mice (Figure 2B; CC: n = 46, CW: n = 58, WW: n = 25; CC vs. CW: $P < 0.05$, CC vs. WW: $P < 0.001$, CW vs. WW: $P < 0.001$), demonstrating that CW and WW mice are more susceptible to thermal challenge than their CC littermates. Prolonged ECoG monitoring of CW and wild-type CC mice did not reveal any interictal epileptiform activity or subclinical seizures; similarly, most patients with the β1(C121W) mutation do not have interictal EEG abnormalities (4). These data indicate that the heterozygous β1(C121W) mutant mice recapitulate FS seen in patients harboring the same mutation.

In contrast, the phenotype observed in WW mice is much more dramatic, with growth retardation, severe tremors, and spontaneous seizures with a markedly abnormal ECoG, similar to *Scn1b*-knockout mice (16). This growth retardation and perhaps some neurological features may relate to disruption of glucose-stimulated insulin and glucagon release due to disruption of β1-mediated regulation in the pancreas (25).

β1 is an AIS protein. We next examined the precise subcellular distribution of β1 subunits using recombinant adenoassociated viruses (AAV) expressing either β1(C121) or β1(W121) with a C-terminal EGFP tag. The function of a β1 C-terminal YFP-tagged protein has been tested electrophysiologically in a heterologous system and found to be identical to that of untagged β1 (26). In addition, the cytosolic red fluorescent protein, tdTomato, was coexpressed to visualize cellular morphology (27).

Because in situ hybridization has shown particularly high *Scn1b* mRNA levels in the pyramidal cell layers of the hippocampus, upper cortical layers, and the Purkinje cell layer in the cerebellum (14), these areas were targeted for virus-mediated expression. Subsequent to stereotaxic injection of AAV, we studied the subcellular localization of β1(C121)-EGFP. Colabeling the AIS with an antibody directed against AnkyrinG (Ank), a cytomatrix anchoring protein that demarcates the AIS (28), revealed a uniform distribution of membrane-delimited β1(C121)-EGFP along the proximo-distal axis of the AIS (Figure 3, A–D, and Supplemental Figure 2) (13). While small clusters and diffuse cytosolic staining were seen in the soma and proximal dendrites (Figure 3, A–D), membrane-delimited localization was much less obvious compared with the AIS, suggesting that the membrane concentration of β1 in the soma is lower than at the AIS (Supplemental Figure 3). This distribution was identical in principal neurons of all hippocampal subregions (shown for cells in CA3 region and subiculum), cortical pyramidal

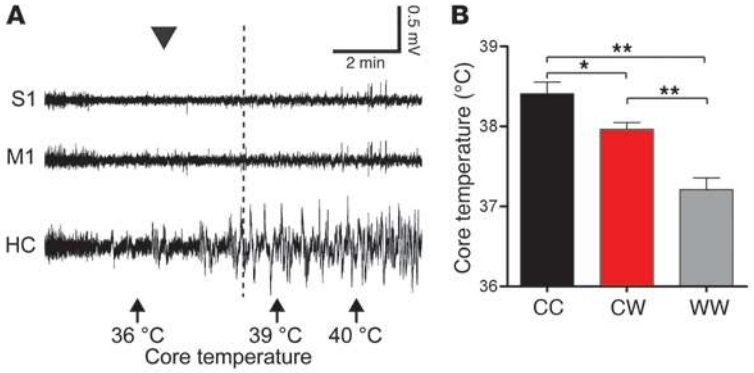

Figure 2

CW mice show FS phenotype. (**A**) ECoGs from somatosensory (S1) and motor cortex (M1) with simultaneous depth recording of hippocampal field potentials (HC). Core temperature increase was nonlinear; selected temperatures are indicated at the bottom. Arrowhead indicates start of heating; dashed vertical line represents start of behavioral arrest phenotype, which occurred at 38.5°C in this mouse. The first signs of epileptiform activity were seen in the hippocampus. (**B**) Thermal seizure threshold is reduced in C121W knockin mice. CC (n = 46), CW (n = 58), WW (n = 25); ANOVA with Bonferroni's post-hoc test; CC versus CW, $^{*}P < 0.05$; CC versus WW, $^{**}P < 0.001$; CW versus WW, $^{**}P < 0.001$.

cells, and cerebellar Purkinje neurons (Figure 3, A–D). As expected, counterstaining using antibodies against Na^+ channel α subunits (Panα) and Ank clearly showed that β1(C121)-EGFP, Na^+ channel α-subunits, and Ank are all present at the AIS and have a similar overlapping distribution (Supplemental Figure 3). Magnification of single confocal frames near the center of the AIS allowed visualization of the plasma membrane and cytosol. β1(C121)-EGFP colocalized with both Na^+ channel α subunits and Ank, and all were AIS membrane delimited (Figure 3E). These observations suggest collectively that native β1 is targeted to the AIS membrane, with less membrane expression in other neuronal compartments.

β1(W121) is not found in the AIS membrane. β1(W121)-EGFP expression revealed a dramatically different distribution compared with wild-type expression (Figure 3, F–I, and Supplemental Figure 2). β1(W121)-EGFP was not detected in AIS membranes (Figure 3, F–I, and Supplemental Figure 2), although it was occasionally found in small clusters within the cytosol of the AIS (Figure 3J). These β1(W121)-EGFP clusters did not colocalize with Na^+ channel α subunits or Ank (Pearson's colocalization coefficients: wild-type β1-EGFP and Ank, 0.64 ± 0.09; β1(121W)-EGFP and Ank, 0.21 ± 0.11; n = 6 each; Student's t test, $P < 0.0001$; see Methods), indicating intracellular retention of the mutant β1(W121) subunit (Figure 3J). The somatic and dendritic expression pattern was cytosolic, as described for β1(C121)-EGFP (Figure 3, F–I, and Supplemental Figure 3). The presence of mutant subunits did not induce major changes in cellular morphology, as assessed by cytosolic tdTomato staining. Panα and Ank staining patterns were also identical to those seen in neurons expressing the β1(C121) subunit (Figure 3, F–J).

These results show that wild-type β1(C121)-EGFP localizes preferentially to the neuronal AIS membrane and that this preferential targeting is disrupted for mutant β1(W121)-EGFP. This suggests that the C121W mutation may cause an AIS-specific pathophysiology (Figure 3, F–I, and ref. 29).

The CW mutation does not affect AIS targeting of Na^+ channel α subunits. In order to assess whether the exclusion of mutant β1(W121) subunits from the AIS has an impact on trafficking of the pore-forming Na^+ channel α subunits, we examined the detailed distribution of the 3 α subunits known to reside in the AIS, $Na_v1.1$, $Na_v1.2$, and $Na_v1.6$ (28, 30–32). In tissue from wild-type CC mice, the distributions of these α subunits were similar to previous reports. $Na_v1.1$ was not found in pyramidal neurons and was exclusively found to localize to the proximal part of the AIS of inhibitory neurons (Figure 4A) (refs. 30, 33; but also see ref. 31). In pyramidal neurons, $Na_v1.2$ was distributed evenly along the AIS (Figure 4B) (28) and was found in pyramidal neurons across the entire hippocampus, whereas $Na_v1.6$ was concentrated in the distal region of the AIS (Figure 4C) (30, 31). Interestingly, neither Na^+ channel nor Ank distributions were changed in tissue from heterozygous CW (data not shown) or homozygous WW mice (Figure 4, D–F). AIS morphology, length, and diameter were also identical in CC, CW, and WW tissue (Supplemental Figure 3). These results show that exclusion of β1 subunits from the AIS due to homozygous C121W mutations does not affect α subunit targeting. This raised the following question: how does the absence of mutant β1(121W) from the AIS membrane impact the functional properties of the neurons and, specifically, of the AIS?

CW neurons are more excitable. We focused our functional experiments on heterozygous CW mice, because human GEFS+ families with *SCN1B* mutations display autosomal dominant inheritance (4), with a single mutant allele sufficient for expression of FS. Subicular pyramidal neurons were chosen because they are implicated in epileptogenesis and display burst firing and single spike firing that may be differentially impacted by the β1(C121W) mutation. As described previously (34), we found that most subicular pyramidal neurons generated initial intrinsic bursts to current injections (400 ms current steps in 20 pA increments, –100 pA to +280 pA, at 34°C), thereafter displaying tonic firing (Figure 5, A and B, and Supplemental Figure 4).

There was no difference in the total number of burst events (n = 13 neurons each; P = 0.74) and the frequency of APs within bursts (n = 13 neurons each; P = 0.33) when comparing CC and CW neurons (Supplemental Figure 4). However, the average burst duration was longer for CW neurons (Figure 5C; P = 0.038 or less for multiple Student's t tests; population average, P = 0.0019) with a concomitant increase in the number of APs per burst (Figure 5D; P = 0.0065).

Subsequent to the burst, the tonic firing frequency was increased in CW compared with CC mice (Figure 5E; P = 0.019 or less for multiple Student's t tests). Accordingly, input-output (I/O) curves showed a significantly increased spike gain in CW neurons for drive currents of less than 150 pA (Supplemental Figure 4; P = 0.0041 or less for multiple Student's t tests). In addition, CW neurons begin to fire APs at lower drive currents than CC cells (Supplemental Figure 4; 60–80 pA).

For the next series of experiments, the first AP in each sweep was analyzed (termed *first AP* hereafter, see Methods). The threshold for AP initiation measured for first APs was on average 2.7 mV more negative in CW compared with CC cells (Figure 5F; CC, –48.7 ± 0.3 mV, CW, –51.4 ± 0.2 mV; CC, n = 121 APs, CW, n = 140; $P < 0.0001$). The amplitude of first APs was significantly higher in CW mice (Figure 6A; CC, 85.28 ± 0.2914 mV, CW, 97.52 ± 0.1081 mV; CC, n = 97 APs, CW, n = 118; $P < 0.0001$). Within each genotype, first AP half-

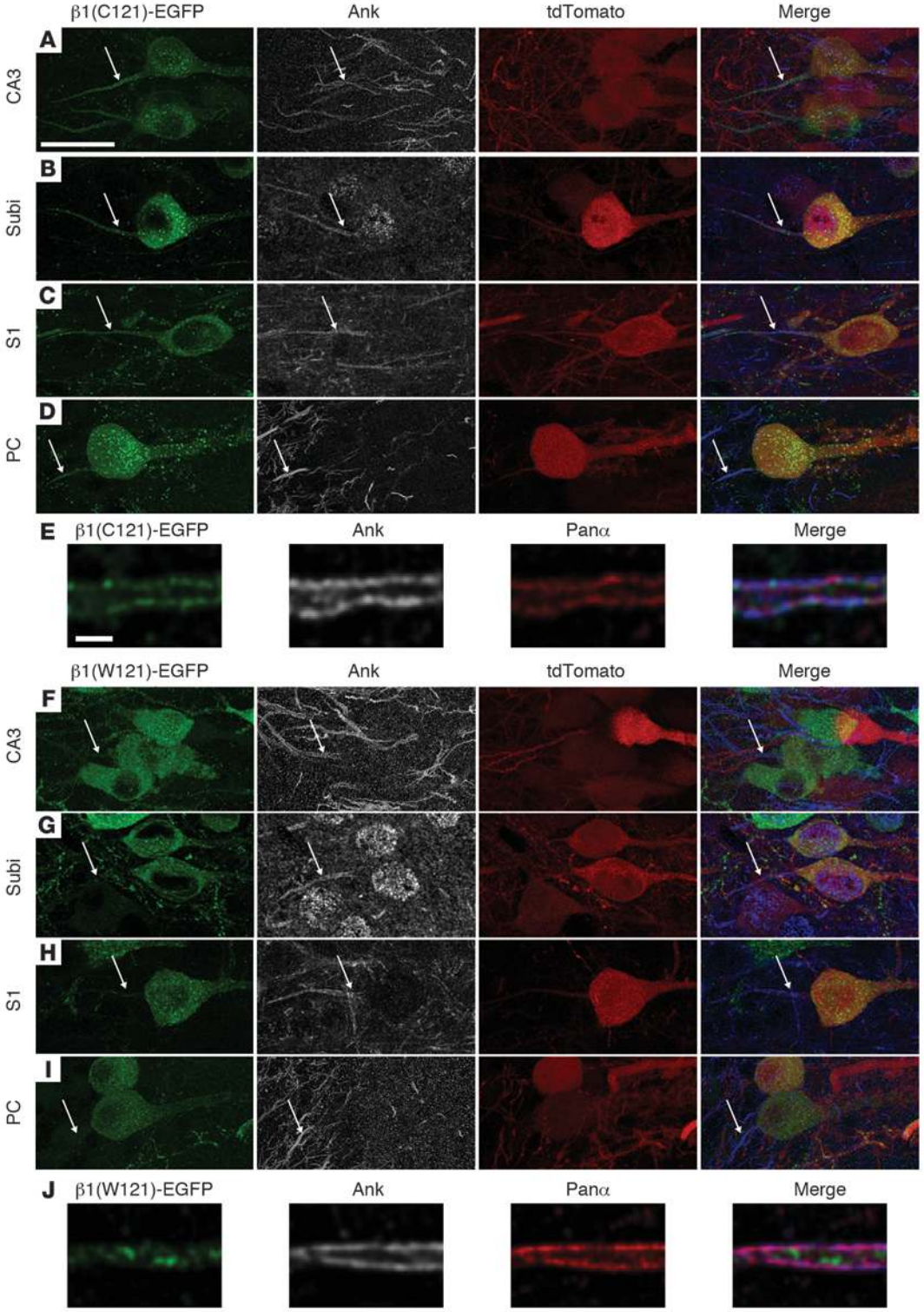

Figure 3

The AIS localization of β1 is disrupted by the C121W mutation. Green indicates virally expressed β1(C121)-EGFP (**A**–**E**) or mutant β1(W121)-EGFP (**F**–**J**). Gray shows AIS visualized by immunostaining against Ank. Red shows virally expressed tdTomato (**A**–**D** and **F**–**I**) or Panα staining (**E** and **J**). Merge of the 3 channels with Ank is depicted in blue. (**A**) Pyramidal neurons in CA3 region of the hippocampus. (**B**) Pyramidal neurons in hippocampal subiculum (Subi). (**C**) Layer 2/3 pyramidal neuron in primary somatosensory cortex (S1). (**D**) Purkinje cell (PC) in cerebellum. Arrows indicate AIS containing β1(C121)-EGFP. (**E**) High magnification of plasma membrane delineating the AIS in a CA3 pyramidal neuron; membrane colocalization of β1(C121)-EGFP with Na^+ channel α subunits and Ank. (**F**–**I**) As in **A**–**D** for β1(W121)-EGFP. Arrows show that β1(W121) does not localize to AIS, identified by anti-Ank staining. (**J**) Proximal β1(W121)-EGFP clusters do not colocalize with Na^+ channel α subunits or Ank, indicating intracellular retention. Scale bars: 20 μm (**A**–**D**, **F**–**I**); 1 μm (**E** and **J**).

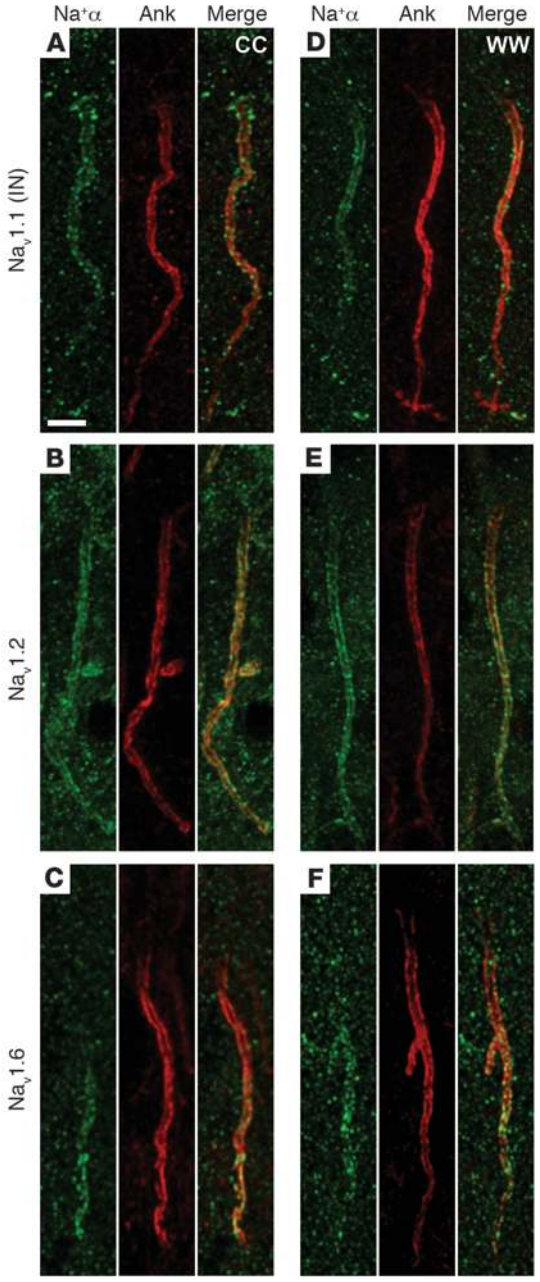

Figure 4
The β1(C121W) mutation does not affect AIS targeting of α subunits. Green shows staining against Na^+ channel α subunit; red shows staining against Ank. Left columns, wild-type (CC) tissue; right columns, homozygous mutant (WW) tissue. (**A** and **D**) $Na_V1.1$ in proximal axon of inhibitory neuron (IN, molecular layer in hippocampus). (**B** and **E**) $Na_V1.2$ is evenly distributed in pyramidal cell AIS (CA3). (**C** and **F**) $Na_V1.6$ gradient with maximum in distal AIS (the "appendage" visible in **F** is an AIS crossing in close proximity, CA3). Scale bar: 5 μm

width did not vary with driving current (Supplemental Figure 4). Comparison of first APs pooled across all driving currents showed that AP half-width in CW neurons was significantly reduced compared with CC neurons (CC, 0.91 ± 0.01 ms, CW, 0.85 ± 0.01 ms; CC, n = 121 APs, CW, n = 140; P = 0.002). Normalization of average CC and CW first APs to maximum amplitude revealed that spikes from neurons of CW reached peak amplitude in a shorter period than CC APs (Supplemental Figure 4).

Taken together, these results show that CW neurons exhibit altered AP initiation indicative of axonal hyperexcitability, increased spike gain, and increased burst firing.

Altered AIS AP initiation in CW mice. Because the data so far suggested that the β1(C121W) mutation gives rise to a selective change in AIS molecular composition and because the AIS is the site for AP initiation in most neurons (19–21, 35), we next made a detailed examination of AP initiation. Two phases of initiation are revealed readily in the second derivative of the AP (d^2V/dt^2; Figure 6, B and C), as described previously for other neuron types (20, 21). The first phase of AP upstroke is due to spike propagation from the AIS into the soma (Figure 6B), while the second phase is caused by generation of the somatic AP (Figure 6B) (20, 21). Figure 6 illustrates a significant increase of the membrane voltage acceleration in the first peak corresponding to AP initiation in the AIS of CW neurons (Figure 6, B, C, and E; CC, n = 103 APs, CW, n = 124; P < 0.0001). At the same time, the subsequent somatic component of the second derivative was unchanged (Figure 6, B, C, and E; CC, n = 103 APs, CW, n = 124; P = 0.51). Finally, there was a small but highly significant increase in the latency between the AIS and somatic AP acceleration peaks, indicating a longer latency in CW neurons between AIS spike initiation and somatic invasion (Figure 6F; P < 0.0001). The phase-plot (Figure 6D) confirms this change in AP kinetics and also better displays the profound change in the AP trajectory in CW neurons. Collectively, these data support the notion of an AIS-specific change in CW mice.

The temperature sensitivity of AIS kinetics was next assessed by recording APs at reduced temperature (22°C) and then comparing with the recordings performed at 34°C as shown above (Figure 6, B and G). Previously, it has been shown that Na^+ channel gating rates increase with increasing temperature (32) and consequently, the kinetics of APs recorded at low temperatures are expected to be slower than APs recorded at higher temperatures. Accordingly, we found that at 22°C recording temperature, the membrane voltage acceleration was lower (Supplemental Figure 5) and AIS to soma delay was increased (Figure 6G). Unlike recordings made at 34°C, there was no significant difference in the AIS peaks between the 2 genotypes recorded at 22°C (Figure 6G; P = 0.91). This result suggests that an increase in temperature increases AIS excitability in both wild-type and CW neurons; however, this increase is significantly larger in CW cells, indicating that the CW mutation renders the AIS more temperature sensitive. This specific increase in temperature gain may lead to the increased susceptibility to FS seen in both patients and the mouse model.

Modeling predicts that wild-type β1 subunits reduce the voltage-dependent opening of AIS Na^+ channels. The most parsimonious explanation for these results is a temperature-sensitive increase in excitability at the AIS in *Scn1b* mutant mice. AIS excitability is determined by differential density of AIS Na^+ currents as well as their voltage-dependent activation (36, 37). The relative influence of these parameters was explored using a computational model in which we systematically altered the midpoint of the activation curve ($V_{1/2}$) of the transient Na^+ current in the AIS. We performed initial experiments in a model neuron with an AIS to soma Na^+ conductance ratio of 15. Shifting voltage-dependent activation of the AIS Na^+ conductance to more hyperpolarized potentials relative to the soma

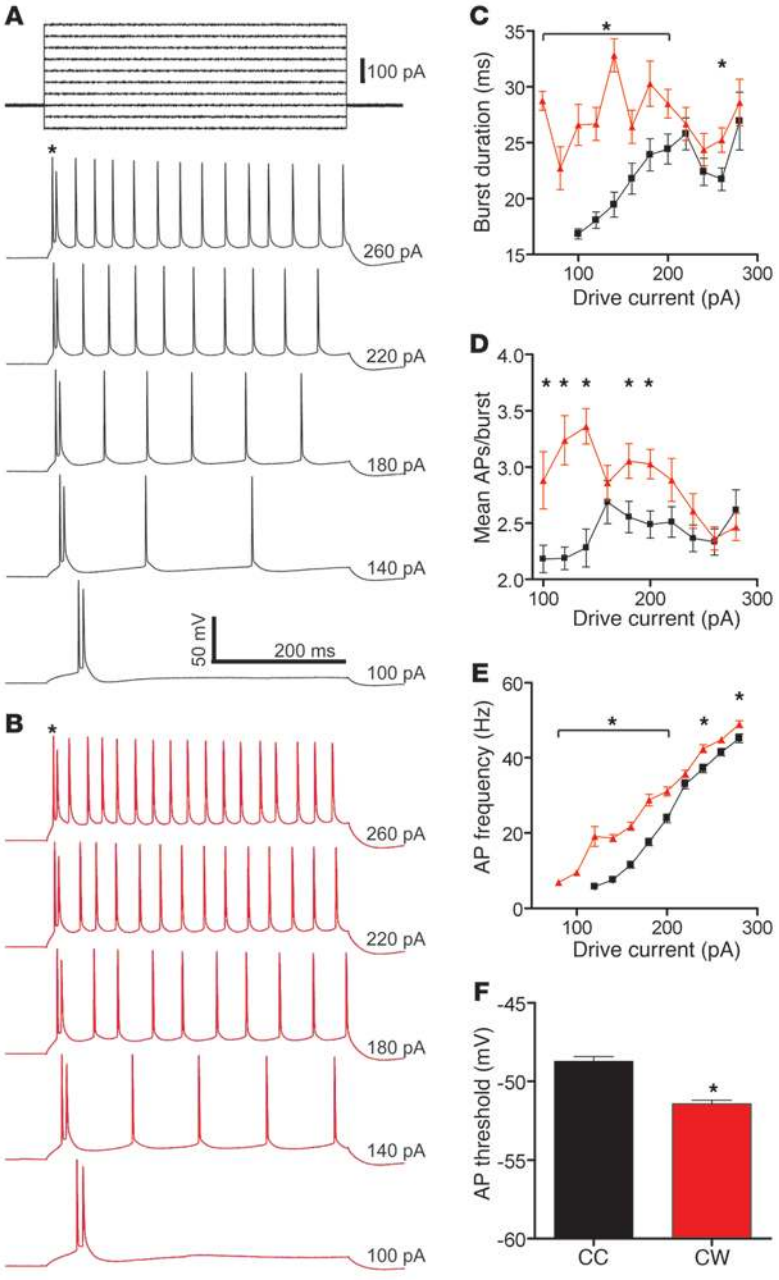

Figure 5
CW neurons are more excitable. Black bars/squares: CC, n = 13 neurons from 8 mice; red bars/ triangles: CW, n = 13 neurons from 6 mice. (**A**) Representative example traces for selected drive currents of a CC subicular neuron. Asterisk indicates burst at beginning of current step. Complete current step protocol used shown at top. (**B**) As **A** but for CW cell. (**C**) Duration of burst events (*P = 0.038 or less for multiple Student's t tests; population average P = 0.0019). (**D**) Number of spikes per burst (*P = 0.025 or less for multiple Student's t tests; population average P = 0.0065). (**E**) Frequency of tonic firing increased in CW cells (*P = 0.019 or less for multiple Student's t tests). (**F**) AP threshold determined for first AP in each sweep (averaged across driving currents; CC, –48.74 ± 0.32 mV; CW, –51.43 ± 0.23 mV; CC, n = 121 APs; CW, n = 140; Mann-Whitney U test, *P < 0.0001).

revealed a striking hyperpolarizing shift in AP threshold (Figure 7A). Furthermore, the AIS membrane potential acceleration and AIS to soma delay also increased with hyperpolarizing changes in $V_{1/2}$ of Na^+ conductance (Figure 7B). These changes in AP properties mirror the physiological changes seen in the CW neurons as compared with CC controls.

A sensitivity analysis of the model was undertaken at a range of conductance ratios from 1 to 15 (AIS/soma Na^+ conductance; Figure 7, C–E). AP threshold varied strongly with $V_{1/2}$ of the AIS Na^+ conductance and in a less pronounced manner with the AIS/somatic conductance ratio (Supplemental Figure 5). The effect of $V_{1/2}$ on the AIS acceleration peak was greater with increasing conductance ratio (Figure 7C). Interestingly, the effect of $V_{1/2}$ on the somatic acceleration peak decreased with increasing conductance ratio (Figure 7D). This suggests that at realistic AIS/soma conductance ratios (approximately 15–20) (36, 37), selective modulation of $V_{1/2}$ at the AIS only affects AIS acceleration and spares the somatic acceleration, which is similar to the physiological data shown in Figure 6. The axo-somatic conduction latency was clearly increased with increasing shift in $V_{1/2}$ over a range of densities (Figure 7E). Collectively, these modeling results indicate that a shift in $V_{1/2}$ of AIS Na^+ channels can serve as a unifying mechanism, explaining the major changes in AP initiation seen in CW mice.

Discussion

Despite a growing body of basic and clinical data, the precise physiological and pathological role of the Na^+ channel β1 subunit has remained elusive. Here, we present a β1(C121W) knockin mouse model that provides insight into the function of the β1 subunit in modulating neuronal excitability and reveals what we believe is a novel mechanism of increased human seizure susceptibility.

In extension of previous data showing AIS localization of β1 in cerebellar neurons (13), we provide evidence that β1 localizes to neuronal AIS membranes in all cell types examined, including cortical and hippocampal neurons. β1 is thus well positioned to modulate the α subunits that are concentrated at the AIS (28, 37). Furthermore, the β1(C121W) mutation causes a striking change in the subcellular localization of mutant β1 subunits, completely disrupting AIS membrane targeting. Contrary to other studies (13, 16), the subcellular localization of Na^+ channel α subunits was not affected by disruption of β1. Our results are consistent with data showing that Ank-binding motifs in Na^+ channel α subunits are both necessary and sufficient for AIS targeting (38). In addition, discrepancies between recent findings in cerebellar neurons may be due to cell-type–specific roles of β1, and the reduction of $Na_V1.6$ expression in only approximately 50% of Purkinje cells suggests the existence of an additional, β1-independent AIS-targeting mechanism (13).

Interestingly the majority of reported disease-causing mutations of β1 (C121W, R85C, R85H, R125C, E87Q I70_E74del) (3, 4, 39, 40) occur within the immunoglobulin-like domain. This domain is important in mediating the interaction of β1 with cellular adhesion

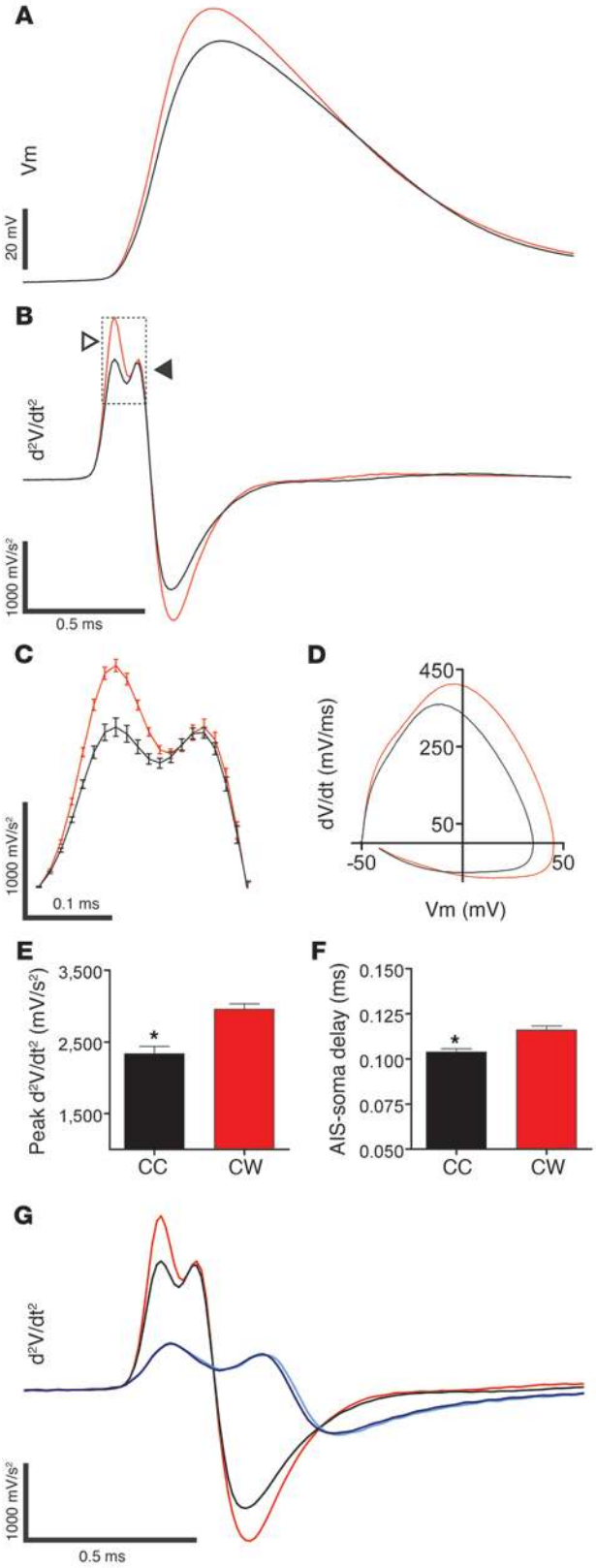

Figure 6
Altered AIS AP initiation in CW mice. Black line/bars: CC, *n* = 13 neurons from 8 mice; red line/bars: CW, *n* = 13 neurons from 6 mice. (**A**) Averaged AP waveforms showing increased amplitude in CW cells (CC, 85.28 ± 0.2914 mV; CW, 97.52 ± 0.1081 mV; amplitude only analyzed for drive currents > 120 pA; CC, *n* = 97 APs; CW, *n* = 118; Mann-Whitney *U* test, $P < 0.0001$). (**B**) Time-aligned second derivative of AP waveform (d^2V/dt^2). (**C**) Magnification of boxed area in **B**; second derivative peaks illustrating significantly increased acceleration and increased peak-to-peak time in CW neurons (error bars represent SEM). (**D**) Comparison of phase plot of AP waveforms (dVdt/ dt) from CC and CW neurons. (**E**) Increased voltage acceleration in CW AIS (CC, *n* = 118 APs; CW, *n* = 139; Mann-Whitney *U* test, $^*P < 0.0001$). (**F**) Increased delay between AIS and somatic peaks (CC, *n* = 103 APs; CW, *n* = 124; Mann-Whitney *U* test; $^*P < 0.0001$). (**G**) Comparison of temperature sensitivity of AIS kinetics. Red solid (CW) and black (CC) lines are recordings made at 34°C as shown in **D**. Blue traces are recordings from the same genotypes but made at 22°C recording temperature (CW, light blue; CC, dark blue; CC, *n* = 71 APs from 8 cells; CW, *n* = 57 APs from 6 cells; $P = 0.91$, Student's *t* test). Time bar: 0.5 ms or 0.1 ms (**C**); Vm bar: 20 mV; $d^2/V/dt^2$ bar: 1000 mV/s^{-2}.

molecules (CAMs) (15, 41) as well as ECM molecules (42) that are found at or in close proximity to the AIS, suggesting that binding of the extracellular domain of β1 to AIS CAMs and ECM molecules is important in sequestering β1 subunits to the AIS, but not to other subcellular compartments. Hence, altered AIS targeting, due to disruption of the immunoglobulin-like domain, may be a common pathogenic pathway in epilepsy patients with underlying β1 mutations. The importance of the immunoglobulin-like domain to targeting is supported by earlier observations on human missense mutations in this domain of the L1 neural cell adhesion molecule (L1CAM), where they disrupt L1CAM surface expression, leading to a variety of congenital neurological syndromes (43).

Viral expression studies suggest that AIS β1 subunits would be reduced in heterozygous CW mice and this reduction may contribute to the observed increases in neuronal and AIS excitability. Our modeling data suggest that the simplest explanation for these results is an increase in excitability of the AIS mediated by an increase in the voltage sensitivity of opening of AIS Na^+ channels. This could be considered a "gain-of-function" change for Na^+ channel α subunits precipitated by the "loss-of-function by absence" of β1(121W) from the AIS membrane. AP threshold changes of only a few mV are sufficient to cause substantial changes in the amount of dendritic input required to trigger APs, and β1 subunits are well positioned to exert this level of control in both excitatory and inhibitory neurons (44).

Indeed, some previous publications show that β1 subunits caused a shift of the voltage dependence of $Na_V1.2$ toward more depolarized potentials (7, 45) consistent with observations in our model, although others did not observe this effect (10, 12, 16). $Na_V1.2$ is widely expressed in pyramidal neurons across the brain including the hippocampus and has been found in both AIS and nodes of Ranvier (28, 32). Although it is fairly well established that $Na_V1.6$ is an abundant brain Na^+ channel thought to mediate AP initiation at the distal end of the AIS (36), little is known about the effects of β1 subunits on this channel (46). Curiously, coexpression of rat β1 with rat $Na_V1.1$ channels, found exclusively in inhibitory neurons, causes a hyperpolarizing shift in activation (47), although this shift was not seen when human β1 subunits were coexpressed with rat $Na_V1.1$ channels (5). This raises the possibility

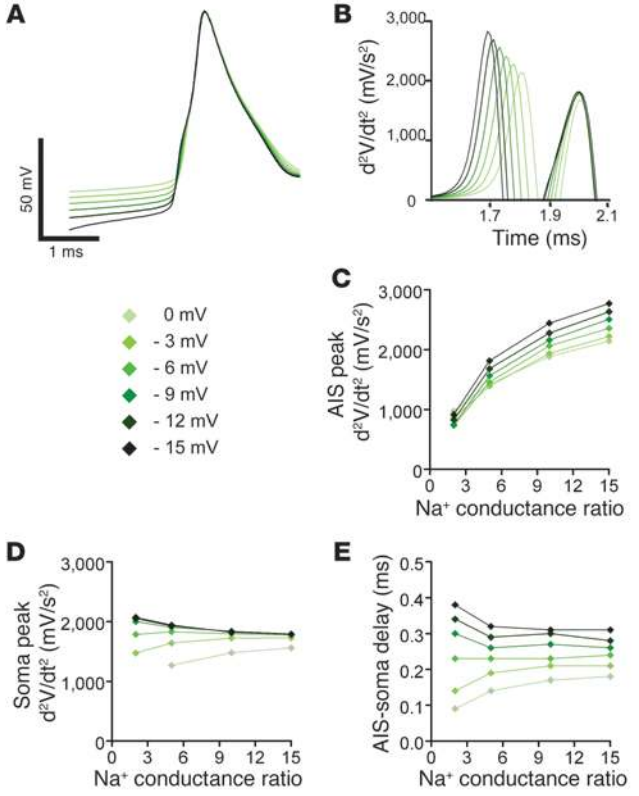

Figure 7
Modeling suggests that wild-type β1 subunits reduce the voltage-dependent opening of AIS Na^+ channels. (**A**) Comparison of first APs elicited by current injection into a neuron model an AIS/soma Na^+ conductance ratio of 15. APs are aligned at threshold as defined for the physiological data. Shifts in AIS Na^+ channel $V_{1/2}$ from 0 to –15 mV are color-coded green to black. $V_{1/2}$ of the soma was held constant. Time bar: 1 ms; Vm bar: 50 mV. (**B**) Second derivative of the voltage traces shown in **A**, illustrating AIS-specific changes in AP initiation (cf. Figure 6, D and E). Traces are aligned to the second peak in the second derivative to more clearly demonstrate changes in peak acceleration and axo-somatic delay. (**C**–**E**) Influence of changes in $V_{1/2}$ of AIS relative Na^+ current density (AIS/soma Na^+ conductance ratios between 2 and 15) on Vm and acceleration reflecting AIS AP initiation (**C**), somatic AP generation (**D**), and axo-somatic delay, calculated as the temporal separation of the 2 peaks in the second derivative (**E**).

that reduced inhibitory neuron excitability may be a contributing factor (13), as proposed for mouse models of Dravet and FS syndromes (33, 48–50). In vitro experiments using human $Na_V1.1$ and rat β1, on the other hand, suggested that β1 acts as a brake on $Na_V1.1$ channel opening by accelerating inactivation, a function that was disrupted by the C121W mutation (17). In the same study, comparison of somatic voltage clamp recordings from *Scn1b* knockout and control Purkinje neurons detected a negative shift in the $V_{1/2}$ of Na^+ channel availability during steady-state inactivation in the knockout but no difference in the voltage dependence of activation. Elucidation of the in vivo role of β1 and precise identification of α subunit partners in various neuronal subtypes and subneuronal compartments would be needed to resolve discrepancies and determine the overall effect on excitability.

The specific impact of the β1(C121W) mutation on AIS function underscores the importance of this neuronal compartment in maintaining normal brain function. Numerous other epilepsy-associated mutations occur in ion channel proteins that are localized to the AIS, including $Na_V1.1$, $Na_V1.2$, and $Na_V1.6$, Ca^{2+} channels, K^+ channels, and GABA receptors (18, 20, 51–54). The convergence of a number of disease genes at the AIS raises the intriguing possibility that several neurological disorders result from AIS-specific pathophysiologies. Given the heterogeneity and complexity of the AIS, the diversity of potential AIS disorders could be quite large (29).

Na^+ channels are the main arbiters of excitation in the nervous system, and we have earlier shown that human $Na_V1.2$ possesses an exquisite temperature sensitivity that implicated it in FS genesis (32). Although the temperature sensitivity of other brain Na^+ channels is not known, this earlier work raises the idea that Na^+ channels themselves may be important participants in FS genesis. We hypothesize that in subicular pyramidal neurons of CW mice, Na^+ channels exist in a state of increased excitability due to reduced amounts of proinhibitory modulation by β1. At normal body temperatures, wild-type β1 produced from the C allele in CW mice may be able to control Na^+ channel excitability, whereas at febrile temperatures, this balance may be disrupted by the combined effects of increasing $Na_V1.2$ conductance and β1 functional null mutation. This idea is supported by our observation that AIS excitability in the heterozygous CW mice is more temperature sensitive than in control CC mice, providing a neuronal compartment level explanation for FS genesis in the CW mice and presumably in patients with this and similar mutations.

In summary, our data implicate β1 as a critical modulator of AIS Na^+ channel function and suggest that an epilepsy-causing mutation can increase excitability and alter temperature sensitivity of this important neuronal compartment. The concentration of epilepsy genes at the AIS further suggests that it may represent an important point of convergence for the pathology of FS and perhaps other epilepsy syndromes as well.

Methods

Construction of the mouse model

CW mice were generated by Ozgene Pty. Ltd. Homologous recombination of a targeting vector made with C57BL/6J-derived genomic DNA was achieved in C57BL/6 Thy1.1 ES cells. The C121W mutation was introduced by PCR together with an EcoRV restriction site, a PGKNeo selection cassette, and 3 loxP sites (Figure 1A). Targeted clones were identified by PCR screening and confirmed with Southern blotting (KI_{fl}; Figure 1B).

Three loxP sites were introduced to generate both CW knockin and knockout mice in parallel. When heterozygous KI_{fl} mice were bred with a Cre-deleter mouse strain, exclusive recombination between loxP sites 1 and 3 yielded only knockout mice. Injection of Cre-expressing plasmid DNA into fertilized eggs (C57BL/6 females × heterozygous KI_{fl} males) was used to obtain better control over Cre levels and yielded all 3 possible loxP recombination events.

For generation of the CW knockin strain, we selected a founder animal with deleted PGKNeo cassette and intact exon 3(C121W) (Figure 1B). After demonstrating the correct recombination event between the second and third loxP site (Figure 1A) using the 5′ probe, the blot was stripped and reprobed for Neo to verify excision of the PGKNeo cassette. In addition, the blot was tested for genomic integration of the Cre-expressing plasmid using a Cre-specific probe (expected band size if Cre is present: approxi-

mately 10 kb). Cre was only transiently expressed, and the plasmid was not integrated into the genome (Figure 1B).

Mice were routinely genotyped by using PCR of tail DNA (Supplemental Figure 1). Experiments were performed using both male and female mice of greater than F6 generation.

ECoG and hippocampal depth recordings

Animal experimentation was approved by the Animal Ethics Committee of the Florey Neuroscience Institutes. Mice were anesthetized with 1%–2% isoflurane and implanted with epidural ECoG electrodes (X lateral of the midline, Y posterior of bregma; S1 X ± 3.0 mm, Y –1.0 mm). Depth electrodes were inserted into the hippocampus at the following coordinates (Z depth from the pia): X ± 2.0 mm, Y –2.0 mm, Z –1.7 mm. Signals were low-pass filtered at 200 Hz, AC-coupled at 0.1 Hz, and sampled at 1 kHz with Powerlab 16/30 (ADInstruments) with synchronized video monitoring using the video capture module. EcoGs were recorded on 3 subsequent days for 3–4 hours per recording session. In a total of approximately 200 hours of mouse ECoGs, we did not see spontaneous epileptiform activity in CC or CW mice.

Thermal seizure testing

P14–P16 mice were exposed to a warm stream of air (<50°C, hair dryer). The core body temperature was simultaneously recorded continuously using a rectal temperature probe. An unresponsive state was defined as the onset of a thermal seizure. In pilot experiments using simultaneous ECoG/depth recordings during thermal seizure induction, we verified that onset of hippocampal epileptiform activity and behavioral arrest coincided. In later experiments, onset of thermal seizures was judged alone by the behavioral state of the mouse. Basal body temperatures of CC and CW mice were similar prior to febrile testing.

Virus particles

We generated AAV1/2-β1(C121)–EGFP and AAV1/2-β1(W121)–EGFP preparations (titer 8×10^6–8×10^7 PFU/ml) using helper plasmids encoding cap1 and cap2 at a ratio of 1:1. Transcription from all AAV constructs was controlled by a hybrid CMV enhancer/chicken β-actin (CBA) promoter. β1(C121) and β1(W121) fusion constructs were designed analogous to those in a previous study (26) with the GFP tag fused to the C terminus of the *Scn1b* (mouse) cDNA with a 6 amino acid Gly-Ser linker. For coexpression experiments, titers of the respective virus solutions were adjusted using PBS. Subsequently, particles coding for EGFP-tagged β1(C121) or β1(W121) and tdTomato were mixed 1:1 and injected together.

Stereotaxic injection

P28 C57BL/6 mice were anesthetized using 1.5% isoflurane. Rectal body temperature was maintained at 36.0–36.5°C with a closed-loop regulated heating pad (FHC Bowdoinham). Stereotaxic injections were performed as previously described (55) at the following coordinates: DG and/or CA1: X ± 1.75 mm, Y – 2.2 mm, Z – 1.8 and – 1.0 mm; CA3: X ± 2.7 mm, Y – 2.2 mm, Z – 1.5 mm; somatosensory cortex: X ± 3.0 mm, Y – 0.5 mm, Z – 1.0 mm; cerebellum: X ± 1.5 mm, Y – 12 mm, Z – 1.5 mm. Calibrated micropipettes (5 μl, intraMARK; Blaubrand) were used to measure the injected volume (50 to 200 nl, depending on the titer). Injected mice were held for 3 to 4 days to allow time for viral expression.

Western blotting

To test specificity of our custom-made rabbit anti-mouse β1 antibody (see below), HEK cells were transfected with cDNA expressing mouse β1-EGFP. The antibody specifically detected a band of 63 kDa in the transfected cultures (Figure 1C). β1 is glycosylated, resulting in a higher than expected molecular weight on the blot (approximately 63 kDa instead of 53 kDa). The faint band in the untransfected control sample was caused by nonspecific binding of the polyclonal antibody at the same molecular weight. In whole-brain extracts of P16 mice, the antibody detected a band of 42 kDa corresponding to native glycosylated β1 protein (Figure 1C) as well as several nonspecific bands at higher molecular weights. Loading controls verified that protein amounts were uniform (data not shown).

Preparation of paraformaldehyde-fixed brain slices and staining methods

Animals were anesthetized with a lethal dose of sodium pentobarbitone (40 mg/kg) and transcardially perfused with 0.1 M phosphate buffer (PB) followed by PB with 1% (specifically used for $Na_V1.1$, 1.2 and 1.6) or 4% paraformaldehyde. The brain was extracted and either (a) immersed in 30% sucrose, frozen, and cut to 20-μm thickness with a freezing microtome ($Na_V1.1$, 1.2 and 1.6) or (b) used to make coronal vibratome sections of 50- to 100-μm thickness. The following antibodies were used: rabbit anti-AnkyrinG (H-215, 1:500; Santa Cruz Biotechnology Inc.), rabbit anti-Na^+ channel subunits (S6936, 1:500, Panα; Sigma-Aldrich), Nav1.1 (clone K74/71; NeuroMab), Nav1.2 (clone K69/3; NeuroMab), Nav1.6 (clone K87A/10; NeuroMab).

In addition, we extensively tested the following antibodies against β1 under various fixation and incubation conditions: 1 commercially available antibody (CA1705, intracellular epitope; Cell Applications), 1 previously published antibody ($β1_{ex}$ antibody; extracellular epitope KRRSETTAETFTEWTFR) (15), and 2 custom-made antibodies raised in 2 different rabbits against the same peptide (extracellular epitopes CKRRSETTAETFTEW). In Western blots, these antibodies showed several nonspecific bands; in addition, they did not recognize recombinant β1-EGFP when virally expressed as positive control in brain sections and did not show specific (sub-)cellular labeling. Hence, we decided to use viral expression methods.

Biocytin-filled cells were ABC-stained using 0.05 % (v/v) 3′,3′-diaminobenzidine (DAB). Sections were mounted on glass slides using SlowFade Light Mounting Medium (Invitrogen).

Confocal laser scanning fluorescence microscopy

Confocal image stacks were acquired with an Olympus FV1000 confocal microscope, equipped with 405 nm, 473 nm, and 559 nm diode lasers, using an Olympus ×60 oil objective (NA 1.35). 3D image stacks were recorded considering Nyquist criteria. Stacks were deconvolved using Huygens Essential software (version 2.31; Scientific Volume Imaging). 3D colocalization between Ank and wild-type β1-EGFP or β1(121W)-EGFP in the AIS was quantified using the Colocalization Analyzer of Huygens Essential. For colocalization analysis, 1–2 AISs in CA3 were selected from 4 different mice per condition. High-resolution Z-stacks were prepared; we used experimentally generated point spread functions for deconvolution and corrected chromatic aberration using Z-stacks of subresolution fluorescent beads to ensure optimal quantification of colocalization. Fluorescence intensity profiles were generated using ImageJ (56).

Biocytin-DAB–stained neurons were imaged in the transmitted light channel of an Olympus FV1000 confocal microscope using a ×20 lens (NA 0.75, air).

Electrophysiology

P14–P16 mice were anesthetized with 2% isoflurane before decapitation. The brain was extracted and 300 μm sagittal vibratome sections were prepared in a saline ice bath. Slices were allowed to recover at room temperature for 1 hour in artificial CSF (aCSF; 125 mM NaCl, 25 mM $NaHCO_2$, 5 mM KCl, 1.25 mM NaH_2PO_4, 10 mM glucose, 1 mM $MgCl_2$, 2 mM $CaCl_2$) bubbled with 95% O_2/5% CO_2.

For current clamp recordings, brain slices were perfused with oxygenated aCSF at 34°C or 22°C. Neurons were visualized and identified with IR-DIC microscopy. The subiculum was located adjacent to the CA1 region of the hippocampus, delineated by lower neuronal density and stratification (Supplemental Figure 4). Pyramidal cells were identified by their larger size (compared with inhibitory neurons) and presence of an apical dendrite.

Somatic whole-cell current-clamp recordings were made with a patch-clamp amplifier (MultiClamp 700A; MDS) using 3–6 MOhm filamented borosilicate micropipettes (GC150F-10; Harvard Instruments) filled with the following solution: 125 mM K-gluconate, 5 mM KCl, 2 mM $MgCl_2$, 10 mM HEPES, 4 mM ATP-Mg, 0.3 mM GTP-Na_2, 10 mM tris-phosphocreatine, 10 mM EGTA (pH 7.2, Osm 290 mosmol). Alexa Fluor 488 fluorescent dye (Invitrogen) and Biocytin (2 mg/ml) were included to allow morphological examination.

Standard capacitance compensation and bridge balance techniques were employed. Membrane resistance was between 50 and 100 MOhm for all recordings. 10 minutes after break-in, pClamp (MDS) was used to drive a current-clamp protocol consisting of 20 current steps of 400 ms duration (20 pA incremental steps from –100 pA to 280 pA) with 300 ms baseline recording on either side of the step. A gap of 500 ms occurred between each sweep. Sampling rate was approximately 83 kHz, equaling 1.2×10^5 s/ data point.

Data analysis

Electrophysiological recordings were analyzed using custom software written in MATLAB (The MathWorks). To minimize the variance of population responses, we selected cells that showed at least 1 burst at the beginning of a current step (Figure 5, A and B; Supplemental Figure 4).

AP analysis. AP baselines were taken from a threshold value defined as 10 $mV.ms^{-1}$, which was also used to align APs for direct comparison. AP peaks were defined as the first local maxima after baseline. AP amplitudes were calculated from peak Vm minus the baseline. To normalize APs of different amplitudes, they were aligned to threshold and scaled to amplitude. Interspike intervals (ISI) were measured as the time between an AP peak and the peak of the previous spike, i.e., the first AP in every "sweep" does not have an associated ISI. Tonic firing was defined as ISI greater than 10 ms. AP full width was determined at half-maximal amplitude (FWHM).

Burst analysis. "Burst events" were characterized by multiple APs in close temporal proximity (ISI < 10 ms), often with reduced amplitude of second/third spike. Burst event duration was measured between the first AP peak and membrane potential crossing the baseline value of the first spike during hyperpolarization at the end of the burst.

Analysis of AP waveforms. The recent history of cellular activity has been shown to affect AP properties such as threshold, width, and amplitude (20). To exclude apparent variation in these parameters due to preceding burst or tonic firing we analyzed the first AP in each sweep ("first AP"); however, we found similar results for spikes in tonic firing mode (data not shown).

AP waveforms were isolated by our custom software (100 data points before AP onset to 150 data points past AP peak). First (dV/dt) and second (d^2V/dt^2) derivatives were calculated numerically. For average AP waveform analysis, APs were aligned to the threshold (10 $mV.ms^{-1}$) in both axes.

Statistics

Data are presented as mean ± SEM. Statistical analysis between 2 independent data sets was performed using a 2-tailed unpaired Student's *t* test using Prism 4.0 (GraphPad Software); $P < 0.05$ was considered significant. Where appropriate, data were tested for normal distribution using the Kolmogorov-Smirnov (KS test) normality test; if data distribution was not normal, nonparametric tests were used. For comparison of multiple data sets, 1-way ANOVA with Bonferroni's post hoc test was used. Survival curves were compared using the log-rank test. Statistical analysis of second derivative waveforms was carried out by semi-automated detection of local maxima/minima. All detections were visually confirmed.

Neuronal modeling

A complex model of a pyramidal neuron was adapted from Royeck et al. (20) and contained biophysically realistic morphology comprising 265 compartments (829 segments) and 15 different distributed Ca^{2+}- and/or voltage-dependent conductances. Implementation was carried out within the NEURON (57) modeling environment running on a dual core processor (2.39 GHz per core, 2 Gb RAM) under Windows XP. Integration time steps were fixed at 0.01 ms. Full details of the model are available at MODELDB (http://senselab.med.yale.edu/modeldb; accession number: 123927). The Na^+ current properties were defined as detailed in the Supplemental Methods.

Acknowledgments

The authors would like to thank Elena Gazina and Nathan Myhill. This work was supported by NHMRC program grant 400121 (to S. Petrou and S.F. Berkovic), by the European Union (contract number LSH-CT-2006-037315, EPICURE, FP6) and BMBF/NGFNplus (01GS08122 to H. Beck; 01GS08123 to H. Lerche), the Deutsche Forschungsgemeinschaft (SFB-TR3 to H. Beck; Le1030/8-2, /10-1 to H. Lerche), the German Science Foundation (to M.T. Horstmann), funding from Bionomics Ltd. (to S. Petrou), and an Australian Research Council Future Fellowship (to C. Reid).

Received for publication January 5, 2010, and accepted in revised form May 26, 2010.

Address correspondence to: Steven Petrou, Florey Neuroscience Institutes, The University of Melbourne, Parkville 3052, Victoria, Australia. Phone: 0061.3.83441957; Fax: 0061.3.93470446; E-mail: spetrou@unimelb.edu.au.

1. Brackenbury WJ, Djamgoz MB, Isom LL. An emerging role for voltage-gated Na+ channels in cellular migration: regulation of central nervous system development and potentiation of invasive cancers. *Neuroscientist*. 2008;14(6):571–583.
2. Brackenbury WJ, Isom LL. Voltage-gated Na+ channels: potential for beta subunits as therapeutic targets. *Expert Opin Ther Targets*. 2008;12(9):1191–1203.
3. Wallace RH, et al. Febrile seizures and generalized epilepsy associated with a mutation in the Na+-channel beta1 subunit gene SCN1B. *Nat Genet*. 1998; 19(4):366–370.
4. Scheffer IE, et al. Temporal lobe epilepsy and GEFS+ phenotypes associated with SCN1B mutations. *Brain*. 2007;130(pt 1):100–109.
5. Patino GA, et al. A functional null mutation of SCN1B in a patient with Dravet syndrome. *J Neurosci*. 2009;29(34):10764–10778.
6. Meadows LS, et al. Functional and biochemical analysis of a sodium channel beta1 subunit mutation responsible for generalized epilepsy with febrile seizures plus type 1. *J Neurosci*. 2002; 22(24):10699–10709.
7. Xu R, et al. Generalized epilepsy with febrile seizures plus-associated sodium channel beta1 subunit mutations severely reduce beta subunit-mediated modulation of sodium channel function. *NeuroScience*. 2007;148(1):164–174.
8. Isom LL, Scheuer T, Brownstein AB, Ragsdale DS, Murphy BJ, Catterall WA. Functional co-expression of the beta 1 and type IIA alpha subunits of sodium channels in a mammalian cell line. *J Biol Chem*. 1995;270(7):3306–3312.
9. Qu Y, Rogers JC, Chen SF, McCormick KA, Scheuer T, Catterall WA. Functional roles of the extracellular segments of the sodium channel alpha subunit in voltage-dependent gating and modulation by beta1 subunits. *J Biol Chem*. 1999;274(46):32647–32654.
10. McEwen DP, Meadows LS, Chen C, Thyagarajan V, Isom LL. Sodium channel beta1 subunit-mediated modulation of Nav1.2 currents and cell surface density is dependent on interactions with contactin and ankyrin. *J Biol Chem*. 2004;279(16):16044–16049.
11. Thomas EA, Xu R, Petrou S. Computational analysis of the R85C and R85H epilepsy mutations in Na+ channel beta1 subunits. *NeuroScience*. 2007; 147(4):1034–1046.
12. Spampanato J, et al. A novel epilepsy mutation in the sodium channel SCN1A identifies a cytoplasmic domain for beta subunit interaction. *J Neurosci*. 2004; 24(44):10022–10034.

13. Brackenbury WJ, et al. Functional reciprocity between Na+ channel Nav1.6 and β1 subunits in the coordinated regulation of excitability and neurite outgrowth. *Proc Natl Acad Sci U S A*. 2010; 107(5):2283–2288.
14. Lein ES, et al. Genome-wide atlas of gene expression in the adult mouse brain. *Nature*. 2007; 445(7124):168–176.
15. Ratcliffe CF, Westenbroek RE, Curtis R, Catterall WA. Sodium channel beta1 and beta3 subunits associate with neurofascin through their extracellular immunoglobulin-like domain. *J Cell Biol*. 2001; 154(2):427–434.
16. Chen C, et al. Mice lacking sodium channel beta1 subunits display defects in neuronal excitability, sodium channel expression, and nodal architecture. *J Neurosci*. 2004;24(16):4030–4042.
17. Aman TK, et al. Regulation of persistent Na current by interactions between {beta} subunits of voltage-gated Na channels. *J Neurosci*. 2009;29(7):2027–2042.
18. Ogawa Y, Rasband MN. The functional organization and assembly of the axon initial segment. *Curr Opin Neurobiol*. 2008;18(3):307–313.
19. Palmer LM, Stuart GJ. Site of action potential initiation in layer 5 pyramidal neurons. *J Neurosci*. 2006;26(6):1854–1863.
20. Royeck M, Horstmann MT, Remy S, Reitze M, Yaari Y, Beck H. Role of axonal NaV1.6 sodium channels in action potential initiation of CA1 pyramidal neurons. *J Neurophysiol*. 2008;100(4):2361–2380.
21. Meeks JP, Mennerick S. Action potential initiation and propagation in CA3 pyramidal axons. *J Neurophysiol*. 2007;97(5):3460–3472.
22. Scheffer IE, Zhang YH, Jansen FE, Dibbens L. Dravet syndrome or genetic (generalized) epilepsy with febrile seizures plus? *Brain Dev*. 2009;31(5):394–400.
23. Dube C, Richichi C, Bender RA, Chung G, Litt B, Baram TZ. Temporal lobe epilepsy after experimental prolonged febrile seizures: prospective analysis. *Brain*. 2006;129(pt 4):911–922.
24. Morimoto T, Nagao H, Sano N, Takahashi M, Matsuda H. Electroencephalographic study of rat hyperthermic seizures. *Epilepsia*. 1991;32(3):289–293.
25. Ernst SJ, Aguilar-Bryan L, Noebels JL. Sodium channel beta1 regulatory subunit deficiency reduces pancreatic islet glucose-stimulated insulin and glucagon secretion. *Endocrinology*. 2009;150(3):1132–1139.
26. Fry M, Porter DM, Maue RA. Adenoviral-mediated expression of functional Na+ channel beta1 subunits tagged with a yellow fluorescent protein. *J Neurosci Res*. 2003;74(5):794–800.
27. Shaner NC, Campbell RE, Steinbach PA, Giepmans BN, Palmer AE, Tsien RY. Improved monomeric red, orange and yellow fluorescent proteins derived from Discosoma sp. red fluorescent protein. *Nat Biotechnol*. 2004;22(12):1567–1572.
28. Van Wart A, Trimmer JS, Matthews G. Polarized distribution of ion channels within microdomains of the axon initial segment. *J Comp Neurol*. 2007; 500(2):339–352.
29. Wimmer VC, Reid CA, So E, Berkovic SF, Petrou S. Axon initial segment dysfunction in epilepsy [published online ahead of print April 7, 2010]. *J Physiol*. doi: 10.1113/jphysiol.2010.188417.
30. Lorincz A, Nusser Z. Cell-type-dependent molecular composition of the axon initial segment. *J Neurosci*. 2008;28(53):14329–14340.
31. Duflocq A, Le Bras B, Bullier E, Couraud F, Davenne M. Nav1.1 is predominantly expressed in nodes of Ranvier and axon initial segments. *Mol Cell Neurosci*. 2008;39(2):180–192.
32. Thomas EA, Hawkins RJ, Richards KL, Xu R, Gazina EV, Petrou S. Heat opens axon initial segment sodium channels: A febrile seizure mechanism? *Ann Neurol*. 2009;66(2):219–226.
33. Ogiwara I, et al. Na(v)1.1 localizes to axons of parvalbumin-positive inhibitory interneurons: a circuit basis for epileptic seizures in mice carrying an Scn1a gene mutation. *J Neurosci*. 2007;27(22):5903–5914.
34. Cooper DC, Chung S, Spruston N. Output-mode transitions are controlled by prolonged inactivation of sodium channels in pyramidal neurons of subiculum. *PLoS Biol*. 2005;3(6):e175.
35. Stuart G, Hausser M. Initiation and spread of sodium action potentials in cerebellar Purkinje cells. *Neuron*. 1994;13(3):703–712.
36. Hu W, Tian C, Li T, Yang M, Hou H, Shu Y. Distinct contributions of Na(v)1.6 and Na(v)1.2 in action potential initiation and backpropagation. *Nat Neurosci*. 2009;12(8):996–1002.
37. Kole MH, Ilschner SU, Kampa BM, Williams SR, Ruben PC, Stuart GJ. Action potential generation requires a high sodium channel density in the axon initial segment. *Nat Neurosci*. 2008;11(2):178–186.
38. Garrido JJ, Fernandes F, Moussif A, Fache MP, Giraud P, Dargent B. Dynamic compartmentalization of the voltage-gated sodium channels in axons. *Biol Cell*. 2003;95(7):437–445.
39. Audenaert D, Claes L, Ceulemans B, Lofgren A, Van Broeckhoven C, De Jonghe P. A deletion in SCN1B is associated with febrile seizures and early-onset absence epilepsy. *Neurology*. 2003;61(6):854–856.
40. Watanabe H, et al. Sodium channel beta1 subunit mutations associated with Brugada syndrome and cardiac conduction disease in humans. *J Clin Invest*. 2008;118(6):2260–2268.
41. McEwen DP, Isom LL. Heterophilic interactions of sodium channel beta1 subunits with axonal and glial cell adhesion molecules. *J Biol Chem*. 2004; 279(50):52744–52752.
42. Xiao ZC, et al. Tenascin-R is a functional modulator of sodium channel beta subunits. *J Biol Chem*. 1999; 274(37):26511–26517.
43. Moulding HD, Martuza RL, Rabkin SD. Clinical mutations in the L1 neural cell adhesion molecule affect cell-surface expression. *J Neurosci*. 2000; 20(15):5696–5702.
44. Kress GJ, Dowling MJ, Eisenman LN, Mennerick S. Axonal sodium channel distribution shapes the depolarized action potential threshold of dentate granule neurons. *Hippocampus*. 2009;20(4):558–571.
45. Qu Y, et al. Differential modulation of sodium channel gating and persistent sodium currents by the beta1, beta2, and beta3 subunits. *Mol Cell Neurosci*. 2001;18(5):570–580.
46. Zhou W, Goldin AL. Use-dependent potentiation of the Nav1.6 sodium channel. *Biophys J*. 2004; 87(6):3862–3872.
47. Barela AJ, et al. An epilepsy mutation in the sodium channel SCN1A that decreases channel excitability. *J Neurosci*. 2006;26(10):2714–2723.
48. Oakley JC, Kalume F, Yu FH, Scheuer T, Catterall WA. Temperature- and age-dependent seizures in a mouse model of severe myoclonic epilepsy in infancy. *Proc Natl Acad Sci U S A*. 2009;106(10):3994–3999.
49. Yu FH, et al. Reduced sodium current in GABAergic interneurons in a mouse model of severe myoclonic epilepsy in infancy. *Nat Neurosci*. 2006; 9(9):1142–1149.
50. Tang B, et al. A BAC transgenic mouse model reveals neuron subtype-specific effects of a Generalized Epilepsy with Febrile Seizures Plus (GEFS+) mutation. *Neurobiol Dis*. 2009;35(1):91–102.
51. Devaux JJ, Kleopa KA, Cooper EC, Scherer SS. KCNQ2 is a nodal K+ channel. *J Neurosci*. 2004; 24(5):1236–1244.
52. Papale LA, et al. Heterozygous mutations of the voltage-gated sodium channel SCN8A are associated with spike-wave discharges and absence epilepsy in mice. *Hum Mol Genet*. 2009;18(9):1633–1641.
53. Bender KJ, Trussell LO. Axon initial segment Ca2+ channels influence action potential generation and timing. *Neuron*. 2009;61(2):259–271.
54. Christie SB, De Blas AL. GABAergic and glutamatergic axons innervate the axon initial segment and organize GABA(A) receptor clusters of cultured hippocampal pyram idal cells. *J Comp Neurol*. 2003;456(4):361–374.
55. Wimmer VC, Nevian T, Kuner T. Targeted in vivo expression of proteins in the calyx of Held. *Pflugers Arch*. 2004;449(3):319–333.
56. Abramoff MD, Magelhaes PJ, Ram SJ. Image Processing with ImageJ. *Biophotonics Int*. 2004;11(7):36–42.
57. Carnevale NT, Hines ML. *The NEURON Book*. New York, New York, USA: Cambridge University Press; 2006.